Biophysical Journal, Volume *115*

Supplemental Information

Antimargination of Microparticles and Platelets in the Vicinity of Branching Vessels

Christian Bächer, Alexander Kihm, Lukas Schrack, Lars Kaestner, Matthias W. Laschke, Christian Wagner, and Stephan Gekle

Supplemental Information - Anti-margination of microparticles and platelets in the vicinity of branching vessels

Christian Bächer[1], A. Kihm[2], L. Schrack[1,3], L. Kaestner[4], M.W. Laschke[5], C. Wagner[2], and S. Gekle[1]

[1]Biofluid Simulation and Modeling, Theoretische Physik, Universität Bayreuth, Bayreuth, Germany
[2]Experimental Physics, Saarland University, Saarbrücken, Germany
[3]Institute for Theoretical Physics, University of Innsbruck, Innsbruck, Austria
[4]Institute for Molecular Cell Biology, Research Centre for Molecular Imaging and Screening, Center for Molecular Signaling (PZMS), Medical Faculty, Saarland University, Homburg/Saar, Germany
[5]Institute for Clinical & Experimental Surgery, Saarland University, Homburg/Saar, Germany

Inflow: full margination and constant particle number

In figure S1 we show the state of complete margination at the entrance of a bifurcating channel and a confluence, respectively. The cross-sectional concentrations show the red blood cells accumulated around the channel center and the microparticles close to the wall.

Figure S2 shows that after a short transient time the implemented particle inflow/outflow leads to a constant number of red blood cells and microparticles in the system.

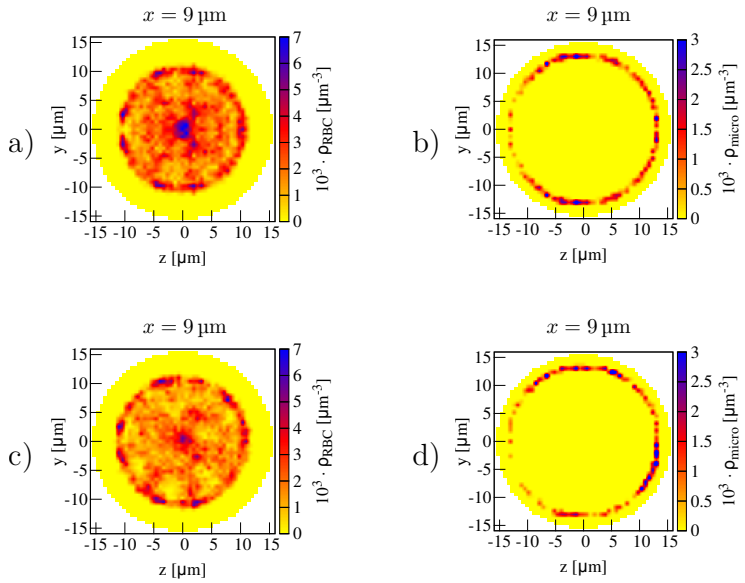

Figure S1: At the entrance of the confluence system a),b) and the bifurcation system c),d) we have a state of full margination: the red blood cells a),c) are located in the channel center, the microparticles b),d) near the wall.

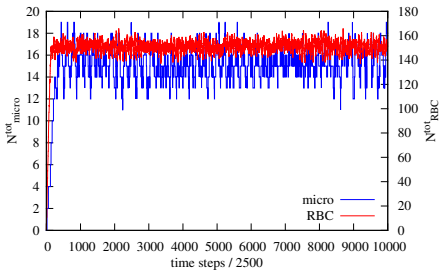

Figure S2: Total number of RBCs and microparticles within the confluence system depending on the simulation time. Both numbers fluctuate around a constant value after initial filling of the system.

Concentration profiles of tracer particles

In order to model the behavior of red blood cells and microparticles we use passive point particles as tracers flowing with the intrinsic velocity profile (1). We first start with the confluence. Homogeneously distributed particles exhibit a similar concentration profile as the red blood cells. As a consequence, red blood cell behavior can be explained by the intrinsic velocity profile. Doing the same calculations for tracers in the different regions resemble the labeled red blood cells. It also fits the concentration profiles for the microparticles.

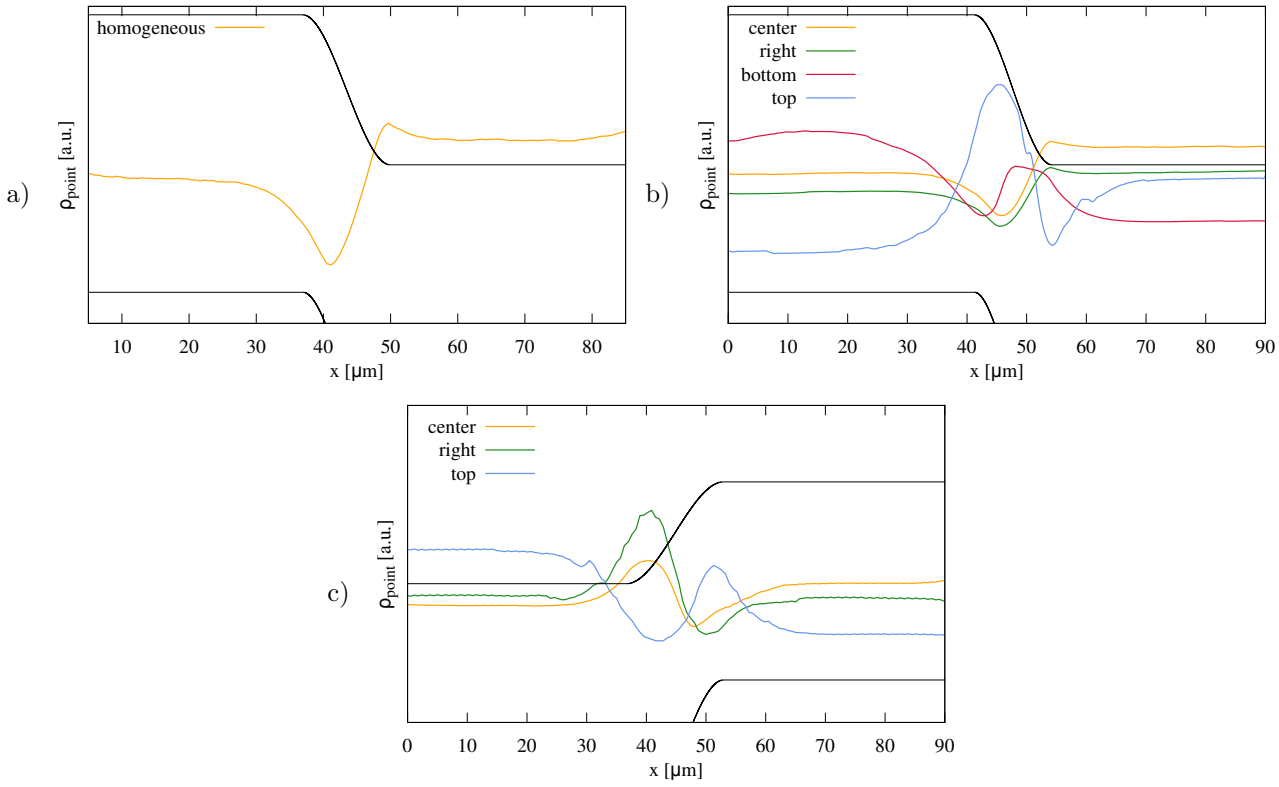

Figure S3: Concentration of a) homogeneously distributed tracer particles and b) tracer particles flowing in the distinct regions at system entrance within the confluence. c) Tracer particles flowing in the distinct regions at system entrance within the diverging bifurcation. These figures are compared to cell and particle concentration in figure 6, 11 and 13 in the main text.

In the diverging bifurcation starting at top the concentration profile of the point particles matches that of the microparticles quite well. Also the point particles located right reproduce microparticle behavior. We note that starting point particles top or bottom and left or right results in the same concentration due to symmetry. Red

blood cell behavior is also similar to that of point particles, except the peak at the bifurcation apex. The differences are effects due to the finite size and deformability of red blood cells.

Shear-induced diffusion

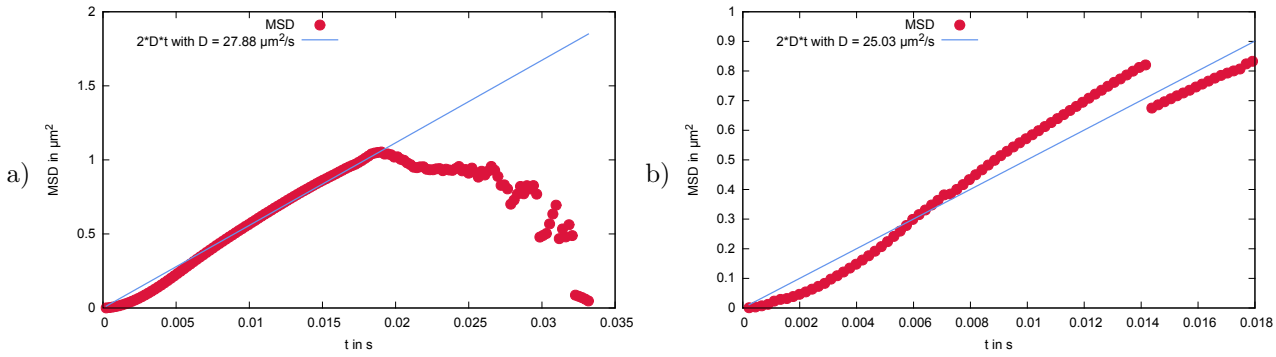

Figure S4: Mean square displacement over time for a) red blood cells and b) microparticles located near the center behind a confluence. By modeling the theoretical expectation we can extract a shear-induced diffusion coefficient.

Larger hematocrit

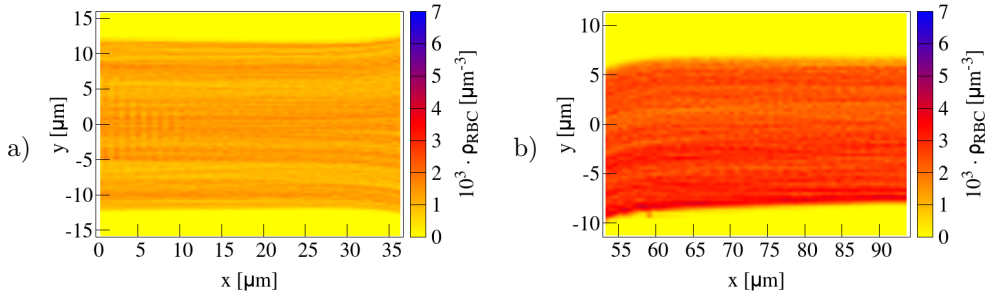

Figure S5: 2D planar projection for red blood cells along the a) main channel and b) branches of the bifurcation with larger hematocrit $Ht = 20\%$. The cell-free layer decreases, but the behavior is qualitatively unchanged.

Anti-margination of platelet-shaped microparticles

In the main text we focus on spherical microparticles. Here, we show additional results for oblate spheroids – a geometry that mimicks more closely that of real platelets. The platelets have a diameter of 3.9 μm along the two long axes and 2.3 μm along the small axis and are illustrated in figure S6. Similar to the spherical particles of the main text, about 14% of the spheroidal microparticles are anti-marginated directly behind the confluence.

Narrow confluence

In figure S7 we investigate the influence of the main vessel diameter. We perform simulations with radius 22.8 μm and 14.3 μm of the main vessel, but with the same branch properties as in figure 1 a) of the main text. In figure S7 a) the red blood cell concentration shows a more stable central cell-free layer for a wider vessel. In case of a narrow vessel the central cell-free layer vanishes more quickly (figure S7 b). Correspondingly, the microparticles stay close

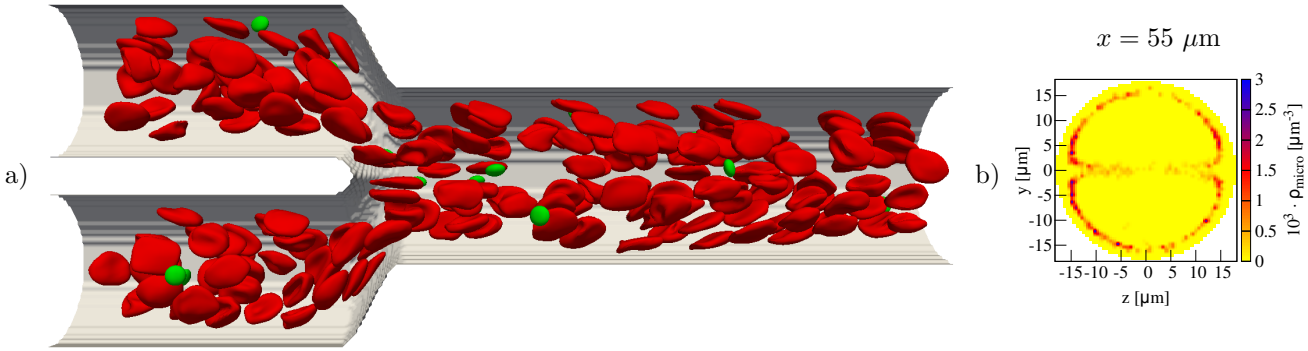

Figure S6: (a) Simulation of microparticles with a platelet-like oblate shape flowing through a confluence. (b) Similar to the spherical microparticles of the main text, these particles also undergo anti-margination.

to the center in the wider vessel (figure S7 c) and marginate faster within the narrow main vessel (figure S7 d). Both observations can be explained by the shear-induced diffusion coefficient depending on the local cell concentration, which increases with narrowing main vessel for the same inflow. Indeed, the red blood cell shear-induced diffusion coefficient decreases in figure S7 a) to 15.5 μm^2/s and increases in figure S7 b) to 45.4 μm^2/s.

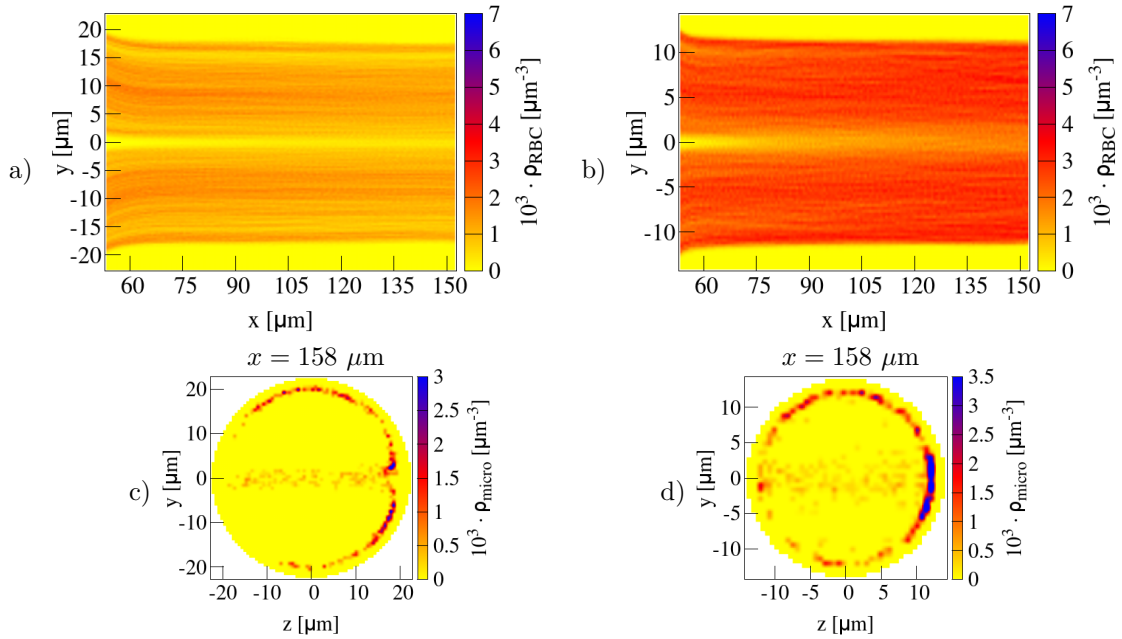

Figure S7: a),b) Red blood cell distribuition and c),d) cross-sectional microparticle concentration 100 μm behind a confluence with main vessel radius of a),c) 22.8 μm and b),d) 14.3 μm. While a wider vessel leads to a more stable central cell-free layer a narrow vessel causes the cell-free layer to smear out faster. Correspondingly, in case of a narrower main channel margination of microparticles takes place faster.

Validation of the used IBM-LBM algorithm

In the following, we summarize and extend the validation for our Immersed Boundary method (IBM) and Lattice-Boltzmann method (LBM). In ref. (2) the calculation of shear and bending forces has been validated for a capsule in shear flow. In ref. (3) the hematocrit profile for tube flow and plane-Poiseuille flow has been shown to agree with previous, established studies. Furthermore, the stability of the stiff spherical particles used has been demonstrated and the flow profile past a sphere has been compared favorably to the analytical solution.

In addition, we here calculate the Stokes drag $1/(6\pi\eta a)$ that relates the force on a sphere of radius a to its velocity in a suspending fluid of viscosity η for a sphere with two different particle resolutions in figure S8. We performed simulations with the resolution used in the main text (81 nodes of the inner stiff grid) and an increased resolution (485 nodes of the inner grid). We note that for the former the number of fluid nodes per particle does not change compared to the main text. Both resolutions show good agreement with the theoretical prediction and convergence to the theory for increasing grid resolution.

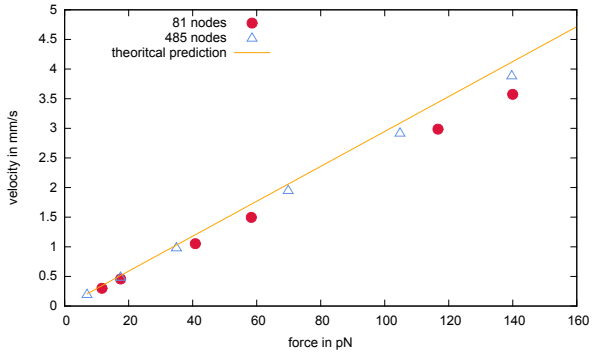

Figure S8: Velocity of a spherical particle pulled through a fluid with a given force. Simulations with two different particle resolutions are compared to the theoretical prediction given by the Stokes drag. The resolution given in the legend denotes the node number of the stiff inner grid.

In order to provide another quantitative validation of stiff particle behavior we simulate a spheroid with aspect ratio $\epsilon = 3$ subjected to shear flow, as sketched in figure S9 a). Ref. (4) provides an analytical solution for the spheroid inclination angle θ over time t

$$\theta(t) = \tan^{-1}\left(\epsilon \tan\left(\frac{t\dot{\gamma}}{\epsilon + \frac{1}{\epsilon}}\right)\right), \tag{S1}$$

with $\dot{\gamma}$ being the shear rate. In figure S9 b) we compare our numerical results (2562 nodes and 5120 triangles for the outer membrane of the spheroid) to the theoretical prediction and find very good agreement.

In order to validate the red blood cell behavior, we present a detailed investigation of a single red blood cell flowing through a cylindrical channel. In figure S10 we show the red blood cell shape obtained for a confinement - effective red blood cell diameter divided by the channel diameter - of 0.55, which can directly be compared to literature data in figure 1 of Fedosov et al. (5). From left to right we increased the dimensionless shear $\dot{\gamma}^* = \bar{\dot{\gamma}}\tau$ with the averaged shear rate $\bar{\dot{\gamma}}$ defined by the averaged velocity over the channel diameter and τ the relaxation time of a red blood cell. Since in this setup the focus is on the single cell behavior we performed our simulations with a membrane mesh resolution of 5120 triangles. With increasing velocity we first observe a tumbling discocyte, a tank-treading slipper, and eventually a croissant. The shapes are in very good agreement with the shapes shown in figure 1 of ref. (5).

Furthermore, we compare the single cell behavior for different resolutions of the red blood cell mesh with simulations using the Boundary Integral method (BIM) in a rectangular channel of cross-section 10 μm x 12 μm in figure S11. The BIM simulations are part of an extensive study on single cell behavior in rectangular channels which demonstrated quantitative agreement with detailed experiments (6). The presently used LBM-IBM method leads to the same shapes as the more sophisticated BIM simulations.

We further validate our method considering the red blood cell behavior in a setup strongly related to those of the main text: we investigate the Zweifach-Fung effect and compare the results with literature data for a bifurcation

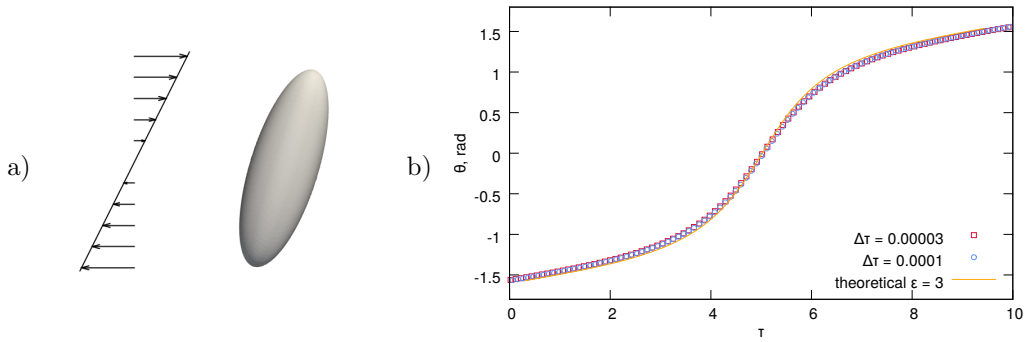

Figure S9: a) A rigid spheroid subjected to a shear flow. b) The orientation angle of the spheroid $\theta(\tau)$ over time $\tau = \dot{\gamma}t$ for simulations with different time steps compared to the analytical solution of ref. (4).

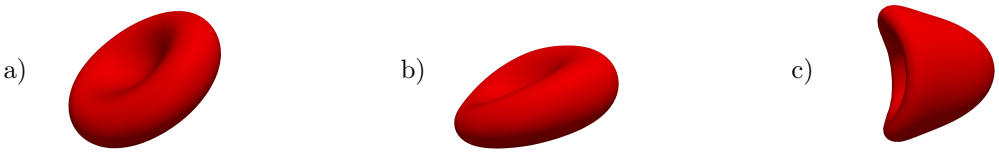

Figure S10: Red blood cell shapes in a cylinder for different flow rates obtained with LBM-IBM simulations. The confinement is 0.55.We observe a) a tumbling discocyte for a shear rate $\dot{\gamma}^* = 5$, b) a slipper for $\dot{\gamma}^* = 22.5$ and c) a croissant for $\dot{\gamma}^* = 60$. These shapes are in very good agreement with the shapes shown in figure 1 of ref. (5) for a confinement of 0.58 and $\dot{\gamma}^* = 5$, $\dot{\gamma}^* = 24.8$, and $\dot{\gamma}^* = 59.6$, respectively, that are obtained using Dissipative Particle Dynamics (5).

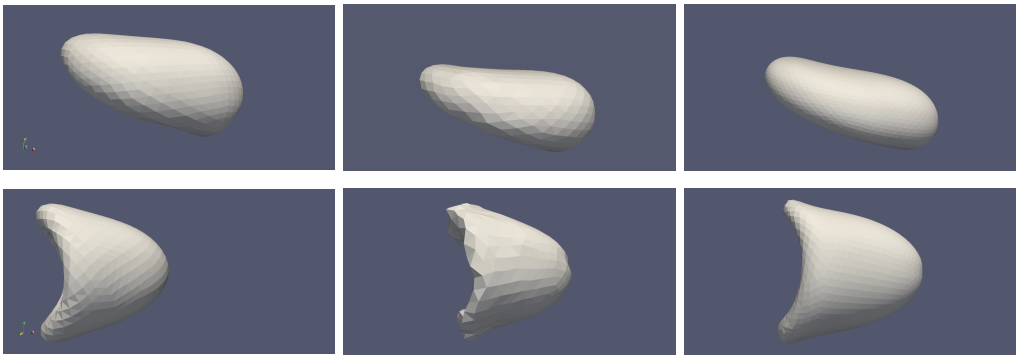

Figure S11: Single red blood cell in a rectangular channel with cross-section 10 μm x 12 μm simulated with the Boundary Integral method from (6), LBM-IBM with 1280 triangles and LBM-IBM 5120 triangles (from left to right). For a centroid velocity of 0.5 mm/s (top) a tank-treading slipper shape is observed and for 1.5 mm/s (bottom) a croissant shape.

of a vessel into two daughter vessels followed by a confluence, as sketched in figure S12 a). In contrast to the main text, here we use periodic boundary conditions. We construct our setup in a way that the cross-sections of the cylindrical branches match with the setup consisting of rectangular vessels of ref. (7), namely the main branch with radius 6.84 μm, the bottom branch with 5.86 μm, and the top branch varied in the range of 3.26 μm to 5.35 μm. We simulate a suspension of 50 red blood cells with a membrane mesh consisting of 642 nodes and 1280 triangles being the same as in the main text. The fluid grid is chosen such that the number of fluid nodes per cell is also the same as in the main text. With varying flow rate ratio between the bottom branch and the main branch (achieved by varying the diameter of the top branch) a disproportional partitioning of the red blood cells takes place, known as the Zweifach-Fung effect (7–9). In order to quantify this behavior in simulations we calculate the fraction of

the flow rate in the bottom branch Q_{bot} and in the main branch Q_m without any cells present. This is done by integrating the axial velocity v_x over the cross-section C of the branch

$$Q_{\mathrm{m}} = \int_C v_x^{\mathrm{m}} \mathrm{d}A, \quad Q_{\mathrm{bot}} = \int_C v_x^{\mathrm{bot}} \mathrm{d}A. \tag{S2}$$

As a measure for the red blood cell flux we calculate the number of red blood cells per time $\dot{N}(t)$ passing through the mid-plane of main branch and bottom branch, respectively, and average over all T time steps

$$n = \langle \dot{N}(t) \rangle_t = \frac{\sum_{i=1}^{T} \dot{N}(t_i) \Delta t}{\sum_{i=1}^{T} \Delta t}. \tag{S3}$$

We compare the fraction of red blood cell flux in bottom and main branch $n_{\mathrm{bot}}/n_{\mathrm{m}}$ to data from the literature in figure S12 b). As done in ref. (7) we compare our results with experimental values from Pries et al. (8) and Yang et al. (10) as well as with the numerical values from Balogh and Bagchi (7). Overall, we find very good agreement and our simulations show the expected half-sigmoidal variation collapsing with literature data over a wide range of flow rate fractions. We note that varying the overall velocity does not affect the results in figure S12.

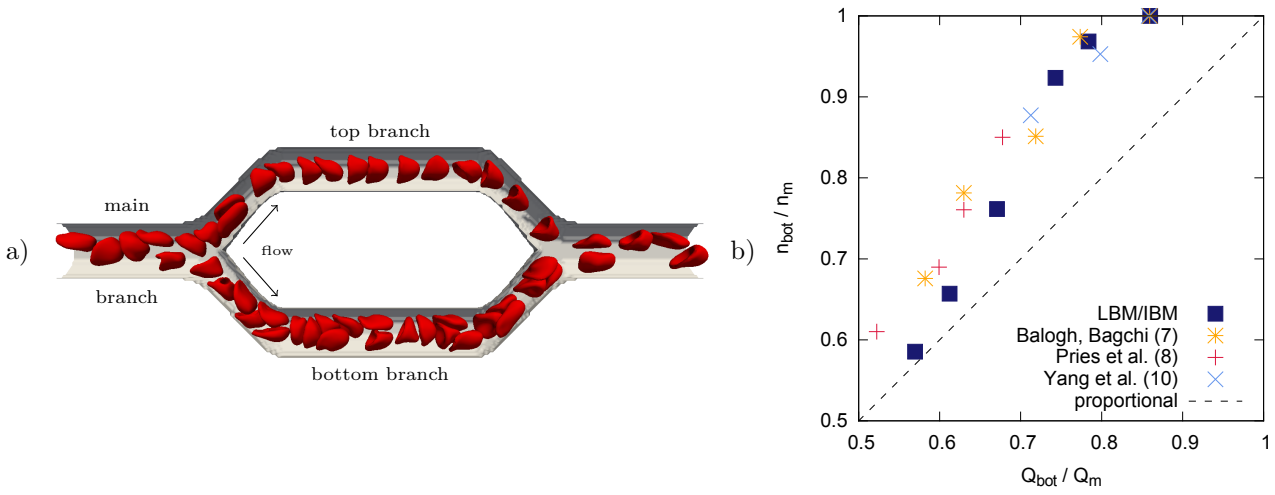

Figure S12: Red blood cells flowing through a bifurcation followed by a confluence. a) Simulation snapshot of one setup: main branch with radius 6.84 μm, bottom branch with radius 5.86 μm, and top branch with radius 5.35 μm. b) Fraction of cells flowing through the bottom branch n_{bot} and the main branch n_{m} depending on the fraction of flow rate in bottom Q_{bot} and main branch Q_{m}. Despite some deviations at low flow rate fraction our simulations lead to the expected half-sigmoidal dependency and match literature data at large fractions.

Next, in order to prove mesh insensitivity we reduced the resolution of the membrane mesh of the red blood cells to 258 nodes and 512 triangles and the resolution of the stiff particles to 66 nodes and 128 triangles. In the same way the fluid mesh changes from 288x110x58 to 200x82x42. The red blood cell distribution behind a confluence and the cross-sectional microparticle concentration are compared to the results of the manuscript in figure S13 a),b) and d),e), respectively. The results are in very good agreement. Small discrepancies may be caused by slightly different inflow concentrations.

Finally, in figure S13 c), f) we provide evidence that the repulsion force among the cells and particles does not affect our results. For this, we show the red blood cell distribution behind a confluence (corresponding to figure S13 b) and the cross-sectional microparticle concentration (corresponding to figure S13 e) for a simulation without repulsion force. We observe very similar behavior and are thus able to conclude that our main results are robust with respect to the repulsion force.

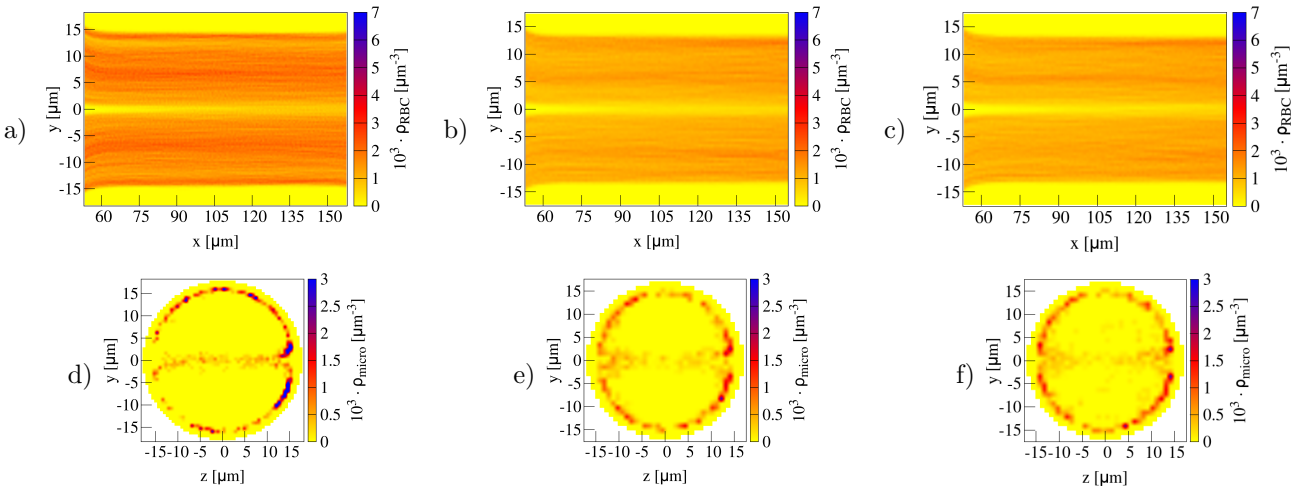

Figure S13: The main results for different mesh resolutions: The cell free-layer in a), b), c) and the microparticle anti-margination in d), e), f). a),d) resolution used in the main text (RBC: 1280, microparticle: 320, fluid: 288x110x58) and b), c), e), f) decreased resolution (RBC: 512, microparticle: 128, fluid: 200x82x42). Both resolutions lead to similar results for central cell free layer stability (in a) and b)) and fraction of anti-marginated microparticles (d) 15.8% and e) 16.2%). In figure c) and f) we provide evidence that without any repulsive force between cells, particles, and the vessel wall our main results do not change (16.7% antimarginated microparticles in f). Figures a) and d) are from the main text.

Taken together, our LBM-IBM method gives accurate results for stiff particles and red blood cells in simple tube flow, but also within a more complex system such as a bifurcation followed by a confluence. We provided evidence that neither the resolution of cell membrane mesh nor the fluid mesh nor the introduced repulsive force for additional stability affect our main results and conclusions.

References

[1] Bächer, C., L. Schrack, and S. Gekle, 2017. Clustering of Microscopic Particles in Constricted Blood Flow. Physical Review Fluids 2:013102.

[2] Guckenberger, A., M. P. Schraml, P. G. Chen, M. Leonetti, and S. Gekle, 2016. On the bending algorithms for soft objects in flows. Computer Physics Communications 207:1–23.

[3] Gekle, S., 2016. Strongly Accelerated Margination of Active Particles in Blood Flow. Biophysical Journal 110:514 – 520.

[4] Jeffery, G. B., 1922. The motion of ellipsoidal particles immersed in a viscous fluid. Proc. R. Soc. Lond. A 102:161–179.

[5] Fedosov, D. A., M. Peltomäki, and G. Gompper, 2014. Deformation and dynamics of red blood cells in flow through cylindrical microchannels. Soft matter 10:4258–4267.

[6] Guckenberger, A., A. Kihm, T. John, C. Wagner, and S. Gekle, 2018. Numerical-experimental observation of shape bistability of red blood cells flowing in a microchannel. Soft Matter 14:2032–2043.

[7] Balogh, P., and P. Bagchi, 2017. A Computational Approach to Modeling Cellular-Scale Blood Flow in Complex Geometry. Journal of Computational Physics 334:280–307.

[8] Pries, A., K. Ley, M. Claassen, and P. Gaehtgens, 1989. Red cell distribution at microvascular bifurcations. Microvascular research 38:81–101.

[9] Secomb, T. W., 2017. Blood Flow in the Microcirculation. Annual Review of Fluid Mechanics 49:443–461.

[10] Yang, S., A. Ündar, and J. D. Zahn, 2006. A microfluidic device for continuous, real time blood plasma separation. Lab on a Chip 6:871–880.